This is a coversheet for the preprint titled:

"Mantle avalanches in a Venus-like stagnant lid planet"

By authors:

Madeleine Kerr[1]*, Dave R. Stegman[1] (@lifetectonic on twitter)

[1]*Institute of Geophysics and Planetary Physics, Scripps Institution of Oceanography, University of California, San Diego, La Jolla, CA, USA*

**corresponding author; contact info: mkerr@ucsd.edu ; dstegman@ucsd.edu*

We are submitting this preprint to EarthArXiv and attest it has NOT been peer reviewed and has NOT yet been submitted to any journal. We plan to submit this paper to Earth and Planetary Physics (http://www.eppcgs.org/) in the coming days, as soon as time permits.

Mantle avalanches in a Venus-like stagnant lid planet

Madeleine Kerr[†], **Dave R. Stegman**[†]

Abstract. Stagnant lid planets are characterized by a globe-encircling, conducting lid that is thick and strong, which leads to reduced global surface heat flows. Consequently, the mantles of such planets can have warmer interiors than Earth, and interestingly, a pyrolitic mantle composition under warmer conditions is predicted to have a distinctly different mantle transition zone compared to the present-day Earth (Hirose, 2002; Stixrude and Lithgow-Bertelloni, 2011; Ichikawa et al., 2014; Dannberg et al., 2022). Instead of olivine primarily transforming into its higher-pressure polymorphs such as Wadsleyite and then Ringwoodite, at pressures corresponding to 410km and 520km depth in Earth, respectively, it instead transforms into a mineral assemblage of Wadsleyite, Majorite, and Ferropericlase (WMF), and then to Majorite + Ferropericlase (MF), before finally transforming into Bridgmanite at pressures corresponding to 660km depth in Earth (Stixrude and Lithgow-Bertelloni, 2011; Ichikawa et al., 2014). Convective motions in stagnant lid planets are dominated by small-scale instabilities (cold drips) forming within the mobile rheological sublayer under the rigid lid. Using ASPECT and a thermodynamic model of a pyrolitic mantle composition generated by HeFESTo, we show that under certain conditions, the small drips can pond atop the WMF-MF mineral phase transition. The barrier to convective flow arises from an exotic property of WMF assemblage having a negative thermal expansivity. In contrast to mobile lid planets that recycle their entire lithosphere via large-scale downwellings which pass through the WMF zone without difficulty (Dannberg et al., 2022; Li et al., 2024), the WMF zone in stagnant lid planets is capable of causing an ephemeral layering of the mantle. Our numerical models show that in stagnant lid planets with mantle potential temperatures that exceed 1900K, the smaller, cold drips from the lid continue to pile up until enough of them have coalesced that they collectively avalanche as a larger instability into the deeper interior.

1. Introduction

Despite sharing many similarities, for example forming in close proximity to each other, having similar radii, and both having differentiated into a metallic core surrounded by a silicate mantle, Earth and Venus have a profoundly different expression of tectonism and volcanism on their surface. Plate tectonics on Earth provides a conceptual framework for understanding how the planet's outermost layer, the lithosphere, is broken into tectonic plates which are themselves the surface manifestation of planetary cooling via mantle convection. In contrast, although Venus's surface indicates widespread volcanism, tectonism, and distinct terranes exist, it remains a mystery how any or all of these features are connected to either each other or the underlying mantle dynamics (Smrekar et al., 2018; Adams et al., 2022; Widemann et al., 2023).

With the absence of plate tectonics on Venus, it is instead believed to be in a stagnant-lid regime, which is characterized by a strong conducting lid encircling the entire planetary surface (Solomatov, 1995). Convection occurs differently beneath a stagnant lid, a lithospheric regime characterized by a thick and strong connected lithosphere that encircles the entire planet. Heat flow out of a stagnant lid is limited, and mantle temperatures can remain higher over longer periods than their mobile lid counterparts. The stagnant lid regime is most appropriate for the smaller, terrestrial bodies such as Mars, Mercury, and the Moon (Solomatov and Moresi, 1996; Thiriet

[†] Institute of Geophysics and Planetary Physics, Scripps Institution of Oceanography, University of California, San Diego, CA, USA. Email: mkerr@ucsd.edu.

et al., 2019), it has also been applied to Venus (Solomatov and Moresi, 1996; 1997; Reese et al., 1999a;b). In a stagnant lid planet, most of the temperature difference between the core to the surface occurs across the stagnant lid, which unlike plate tectonics, does not participate in convection. A thin rheological sublayer underlying the stagnant lid is the thermal boundary layer from where small-scale instabilities form (as cold drips) (Solomatov, 1995). Due to the strong temperature-dependent viscosity of silicates, it's expected that the hot and cold thermal boundary layers have correspondingly smaller viscosity ratios across them (Jellinek et al., 2002). In the case of Venus, topographic rises along the rims of some of Venus's largest coronae, such as Artemis and Quetzalpetlatl, might indicate lithospheric flexure which could arise from subduction (Sandwell and Schubert, 1992; Schubert and Sandwell, 1995; Davaille et al., 2017) or delamination (Adams et al., 2022; 2023). This would indicate Venus' lithosphere may not be perfectly stagnant, but a limited amount of recycling might occur on a regional scale, which would not be inconsistent with interpretations of Venus' resurfacing history (Phillips et al., 1992).

In contrast, Earth is presently in a regime of whole mantle convection with hot plumes from the core-mantle boundary (CMB) such as Iceland and Hawaii and recycling oceanic lithosphere (ie tectonic plates) via subduction back into the mantle. The downwelling flows of colder, denser material associated with the history of subduction likely explain the long wavelength components of Earth's geoid (Lithgow-Bertelloni and Richards, 1998) and are thought to interact with chemically dense piles at the base of the mantle (McNamara and Zhong, 2005; 2004). However, there is evidence via seismic tomography for descending slabs flattening or being deflected between depths of 660 km and 1000 km indicating that some feature of the upper mantle may provide a barrier to flow for cold downwellings (Fukao and Obayashi, 2013; Faccenda and Dal Zilio, 2017).

Early studies focused on whether the phase transition of ringwoodite to bridgmanite plus ferropericlase could cause global layering of the mantle at 660 km depth (Christensen and Yuen, 1984), as this system was considered to have a strongly negative Clapeyron slope, ($\frac{dP}{dT}$), of -6 MPa/K. Subsequent measurements suggested the value was only -3 MPa/K (Ito and Takahashi, 1989; Irifune et al., 1998), which mantle convection models incorporated and reported that only weak or transient layering was possible (Tackley et al., 1993; Honda et al., 1993). Surface kinematics such as trench migration were also shown to play a central role in producing the observed layering of slab structures in the upper mantle (van der Hilst and Seno, 1993; Christensen, 1996), especially in combination with other factors such as bending and sinking mechanics of cold slabs (Čížková et al., 2002; Goes et al., 2017) and mantle viscosity stratification (Yanagisawa et al., 2010).

More contemporary studies suggest the negative Clapeyron slope might be as weak as -1 MPa/K or -0.5 MPa/K (Litasov et al., 2005; Ishii et al., 2011), which would imply the phase change has minimal effect and is therefore not consequential for the origin of slab deflection and flattening. Furthermore, the negative buoyancy of slabs in the mid-mantle could be reduced by other effects such as kinetics of the phase transition within the coldest portions of slabs (King et al., 2015) or if the lower mantle itself is intrinsically denser due to enrichment of basaltic lithologies (Ballmer et al., 2015).

The question of what types of downwellings might exist in Venus' interior and if the mineral phase transitions that occur in Earth's upper mantle could possibly cause layering in Venus' mantle remains unresolved. Some studies have incorporated the ringwoodite to bridgmanite transition in stagnant lid models, typically using values around -2.5 MPa/K (Armann and Tackley, 2012; Huang et al., 2013; Benešová and Čížková, 2012; Rolf et al.,

2018; Uppalapati et al., 2020). Although some of these previous studies report interesting results that may be related to the effects of including phase transitions, mineral physics phase equilibria based on thermodynamics do not predict the same sequence of phase transitions to occur under warmer conditions (Hirose, 2002; Stixrude and Lithgow-Bertelloni, 2011; Ichikawa et al., 2014) which are typically modelled for Venus. For example, if a mantle with a pyrolite composition has a potential temperature that exceeds 1900 K, the associated adiabat crosses into a phase assemblage of wadsleyite, majorite and ferropericlase (WMF) and then into majorite + ferropericlase (MF) (Ichikawa et al., 2014; Dannberg et al., 2022). Thus, the WMF phase assemblage is likely to be more relevant for understanding the dynamics of mantle convection within a stagnant lid planet. A key attribute of the WMF phase assemblage is its exotic thermodynamic property of having a negative thermal expansivity (Dannberg et al., 2022) which has opposite sign relative to all other mantle minerals. Accordingly, hot material in the WMF phase thermally contracts into more dense, negatively buoyant material with respect to ambient mantle, while cold material in the WMF phase thermally expands into less dense, positively buoyant material. Building on recent work (Dannberg et al., 2022; Li et al., 2024), this study will investigate how mantle dynamics are affected by the presence of the WMF phase assemblage and its associated phase transitions in numerical models of mantle convection with conditions appropriate for Venus.

2. Model Description

To investigate the effect of unusual mineral assemblages predicted for warmer mantles under the conditions of a stagnant lid planet, we employ the geodynamic code ASPECT (Bangerth et al., 2020), which can numerically model mantle convection. We adopt the recently developed methodology for modeling phase transitions in thermal convection using entropy (Dannberg et al., 2022) which brings novel improvements to modeling sharp phase transitions and the effects of compressiblity. This new methodology provides several advantages over previous approaches: 1) reformulating the energy equation in terms of entropy instead of temperature, so it becomes continuous at a phase boundary and constant along an adiabat; 2) using the projected density approximation (PDA) to avoid dynamic pressure effects on density to avoid oscillations in the solution while keeping the dynamic effects of temperature (Gassmöller et al., 2020); and 3) readily incorporating a precomputed mineral phase map for a pyrolitic mantle via a look-up table generated by the HeFESTo software which computes thermodynamic phase equilibria for mineral assemblages over the pressure–temperature regime of Earth's mantle (Stixrude and Lithgow-Bertelloni, 2011). The entropy-based method employed in ASPECT allows the dynamic and latent heat effects of both sharp and broad phase transitions to be modelled accurately in a multi-phase assemblage. For more details on those respective methods, see (Dannberg et al., 2022) and (Gassmöller et al., 2020).

2.1. Mineral Phase Assemblages in Warmer Mantles

The equation of state for a pyrolitic mantle is defined by a look-up table, where pressure (p) and entropy (S) are independent variables generated by using the Gibbs free energy minimization software HeFESTo (Stixrude and Lithgow-Bertelloni, 2011; 2005). The specific look-up table used in this study is the one provided in the supporting materials of Dannberg et al. (2022). The table extends from 0-140 GPa in pressure and from 600-3600 J/kg/K in entropy with a resolution in pressure of 100 MPa and 10 J/kg/K in entropy. Figure 1 displays an example of some of the information contained in the look-up table which includes a) thermal expansivity and

b) density values in pressure-temperature space as well as c) pressure variations in density-temperature space. For reference, Fig 1a also provides the adiabatic profiles for mantle potential temperatures between 1600 K to 1900 K in 100 K increments and these 4 adiabats are also displayed as dashed white lines in Fig 1b.

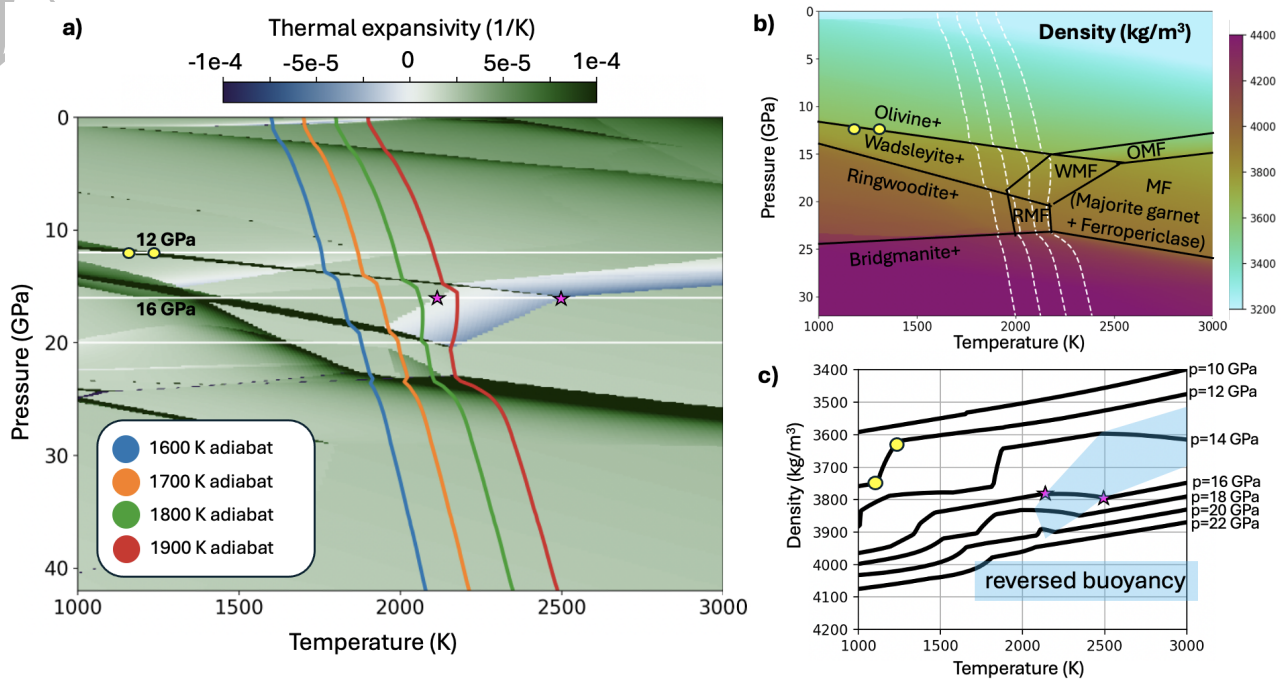

Figure 1: Pressure-temperature maps of a) thermal expansivity (α) and b) density (ρ) of the pyrolitic composition from (Dannberg et al., 2022) overlaid with mantle adiabats for 1600 K, 1700 K, 1800 K, and 1900 K. Plot b) shows the major mineral phases and highlights the transitions between these phases in black. Plot c) shows the density-temperature relation at lines of constant pressure. The light blue highlighted region indicates where increasing temperature at constant pressure increases the density, demonstrating the negative thermal expansivity in effect at that region. The pink stars bound the zone of reversed buoyancy (the WMF phase) at 16 GPa and the yellow circles bound the olivine-wadsleyite transition at 12 GPa.

In Fig 1b we provide a simplified phase diagram (using black lines and dominant mineral indicated) overlying the density field. As can be seen in Figure 1b, descending along the adiabat in a mantle with potential temperature of 1600 K (or lower) represents the nominal transition zone of Earth between 13.5-23 GPa with a characteristic mineralogy dominated by Olivine and its high-pressure polymorphs (Wadsleyite and Ringwoodite) with other minor phases present, before transforming into a Bridgmanite dominated assemlage at 23 GPa. The warmer mantle adiabats each encounter different sequences of phase transitions between 12-25 GPa. Instead of the familiar transition into Ringwoodite, the 1700 K adiabat crosses from the Wadsleyite phase into a mixture of Ringwoodite and Majorite + Ferropericlase (RMF) before converting to Bridgmanite. However, the 1800 K crosses from the Wadsleyite phase first into WMF and then into RMF before converting to Bridgmanite. Along the 1900 K adiabat crosses from Olivine directly into WMF and then descends along the phase boundary between RMF and MF before tranforming to Bridgmanite. The phase map indicates that for the pyrolotic composition,

Majorite garnet + Ferropericlase (MF) is stabilized at the higher temperatures across a broad range of pressures typically dominated by Wadsleyite and Ringwoodite at lower temperatures. Interestingly, there are distinct regions where Olivine, Wadsleyite and Ringwoodite form transitional assemblages, here labeled as OMF, WMF, and RMF, respectively, before reaching the MF stability field. These intermediary mineral assemblages not only lie exactly within the pressure and temperature region of interest for this study, but also exhibit interesting thermodynamic properties. For example, both OMF and WMF have negative thermal expansivity (white and blue region in Fig 1a) as well as WMF and RMF having ∼30-40% larger specific heats (not shown).

The appearance of mineral assemblages with negative thermal expansivity is quite interesting because the dynamics of mantle convection are largely understood as a competition between viscous resisting forces and driving forces arising from the buoyancy generated by the thermal expansion and contraction of varying temperature mantle material. If discrete zones exist in which the thermal expansivity has the opposite sign yet similar magnitude compared to typical mantle materials, the dynamical effects would not be subject to the well-developed intuition from previous studies. As an example, with pressure held constant, mantle materials such as Olivine would normally expand to do an increase in temperature and become less dense. This is exactly the trend seen in the 10 GPa isobar of Figure 1c, in which the positive slope simply reflects the magnitude of thermal expansion. Changes in density can also occur due to phase transformations, as shown by the yellow dots in 1a,b which indicate the temperatures along the 12 GPa isobar for where Olivine has transformed into Wadsleyite and an associated density jump occurs (1c). However, a negative slope along an isobar as indicated by pink stars on the 16 GPa isobar in 1c indicates the typical sense of buoyancy is reversed. This zone of reversed buoyancy is explained by a region of negative thermal expansivity seen in 1a, which directly corresponds to the extent of the WFM phase assemblage 1b. The combined effects of mantle compressibility, density jumps due to phase changes, and thermal expansion that can be either positive or negative can lead to interesting complexities when convective features pass through this pressure range. Consequently, the 4 values of initial mantle potential temperatures shown in 1a essentially offer 4 different planetary mantles based purely on the predicted sequence of mineral phase assemblages and their associated thermodynamic properties.

2.2. Governing equations of thermal convection

Entropy (S), pressure (p), and velocity ($\mathbf{u}$) are solved in a 2D cylindrical annulus using the projected density approximation (PDA) and entropy energy formulation employed in the finite-element geodynamic code ASPECT. The system of equations for bottom-heated thermal convection are:

$$-\nabla \cdot (2\eta\dot{\varepsilon}) + \nabla p = \rho_h \mathbf{g} \tag{1}$$

$$\frac{\partial \rho_h}{\partial t} + \mathbf{u} \cdot \nabla \rho_h + \rho_h \nabla \cdot \mathbf{u} = 0 \tag{2}$$

$$\rho_h T \left(\frac{\partial S}{\partial t} + \mathbf{u} \cdot \nabla S \right) + \rho_h C_p \frac{\partial T}{\partial t}\Big|_{\text{cond}} = 2\eta\dot{\varepsilon} : \dot{\varepsilon}, \tag{3}$$

where variables are defined in Table 1, and $\rho_h = \rho(p_h, T)$ is the density which includes the effect of dynamic changes in temperature but uses the hydrostatic pressure to approximate density (Gassmöller et al., 2020). For this study we do not consider internal heating sources from radioactivity.

Table 1: Variables in thermal convection equations and their values.

Variable	Symbol	Value
velocity	$\mathbf{u}$	model solution [m/s]
temperature	T	from HeFESTo [K]
entropy	S	model solution [J/K]
pressure	p	model solution [Pa]
thermal expansivity	α	from HeFESTo [1/K]
specific heat capacity	C_p	from HeFESTo [J/kg/K]
viscosity	η	computed as reference profile [Pa s]
gravity	g	$8.87\,\mathrm{m/s^2}$
thermal conductivity	k	$4.7\,\mathrm{W/(m}K)$
density	ρ_h	from HeFESTo [kg/m^3]
strain rate	$\dot{\varepsilon}$	model solution [1/s]

2.3. Temperature and depth-dependent viscosity

We model the mantle rheology as a Newtonian fluid with temperature- and depth-dependence. The mantle viscosity in these models is the product of radially and laterally varying components. The radial component of viscosity, $\eta_{rad}(T_A, P)$, is based on the adiabatic mantle temperature profile, $T_A(r)$, using appropriate temperature- and depth-dependent values for an Arrhenius viscosity. This is then multiplied by a factor representing the lateral temperature variation from the adiabat, $\eta_{lat}(T)$, (Steinberger and Calderwood, 2006)

$$\eta(T,P) = \eta_{\text{rad}}(T_A,P)\cdot\eta_{\text{lat}}(T) = A\exp\left[\frac{E_{\text{act}}+P\,V_{\text{act}}}{nR\,T_A}\right]\exp\left[-\frac{H(T-T_A)}{nR(T\,T_A)}\right] \tag{4}$$

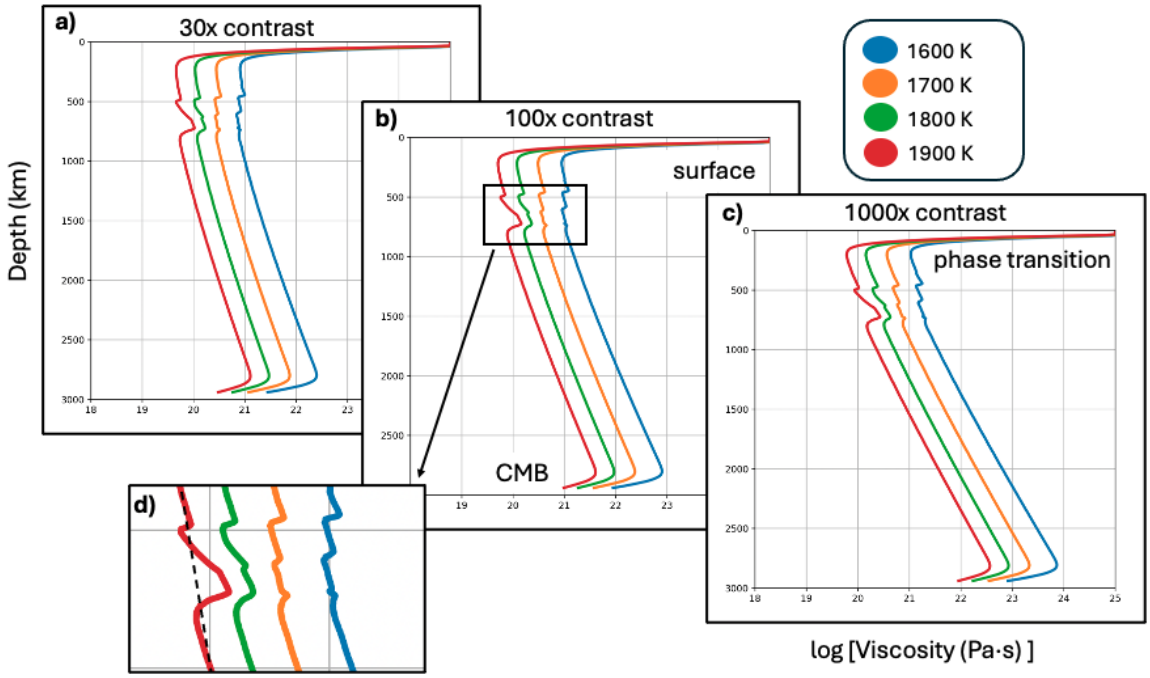

Figure 2: The initial viscosity profiles for models with potential temperatures of 1600 K, 1700 K,1800 K, and 1900 K with varying depth-dependence. Each model has a V_{act} value selected to generate an increase over the depth of the mantle of a) 30x, b) 100x, and c) 1000x. In d) the initial viscosity profiles through the mantle transition zone show a high viscosity ledge at approximately 700 km depth for the 1900 K profile. The black dashed line in d) indicates the linear smoothing from 10-30 GPa applied to the initial viscosity profiles of SL13 and SL14.

where $E_{\text{act}} = 2.4 \times 10^5\, J$, $n = 1$ for the simple case of pure diffusion creep (Karato and Wu, 1993), V_{act} is varied for different viscosity contrasts across the mantle as provided in Table 2, R is the gas constant, and A is the constant which defines the reference viscosity to be 10^{21} Pa·s at 1600 K and $p = 0$. H is the activation enthalpy where $H = E_{\text{act}} + 23 \cdot 10^9\, V_{\text{act}}$ and where $23 \cdot 10^9$ Pa is a common characteristic pressure for mineralogy (corresponding to the 660 discontinuity on Earth). In practice, this viscosity law has both adiabatic temperature and pressure effects in the radial reference profile which are shown in Figure 2 as well as temperature deviations from the adiabat which increase or decrease the viscosity laterally.

One parameter we varied is the degree of viscosity increase throughout the mantle. The parameter controlling this variation, V_{act}, was tuned for each radially-varying reference profile using the adiabatic temperature (T_A), pressure (P), and the Arrhenius viscosity law in equation 4 such that the ratio between the reference surface viscosity and CMB viscosity was 30 (weak), 100 (moderate), or 1000 (extreme).

Another varied parameter was the maximum viscosity which effectively controls the strength of the lithosphere. What we define as mobile-lid models are those with a maximum viscosity of 5×10^{22} Pa·s, as used for Earth models in (Dannberg et al., 2022), which is low enough to allow for the entire lithsophere to become unstable and sink. For stagnant-lid models, a maximum viscosity of 1×10^{25} Pa·s was sufficient to ensure the lithosphere was

entirely rigid.

2.4. Initial and boundary conditions

We adapted the Earth models of (Dannberg et al., 2022) into Venus models by setting the core radius $R_{\text{core}} = 3110\,\text{km}$, the planetary radius to $R_{\text{planet}} = 6052\,\text{km}$, and the gravity to $g = 8.87\frac{\text{m}}{\text{s}^2}$. and Figure 3 shows a summary of the initial conditions and boundary conditions for both the mobile lid (right side) and stagnant lid (left side) models. For both types of models, the inner and outer circular boundaries are free-slip and fixed-temperature (with the temperature enforced by fixing the value of entropy at surface and CMB pressures). The surface entropy is fixed at 1602.822 J/K, corresponding to Venus's surface temperature of 740 K. The mantle's initial state follows along an adiabat that starts with a potential temperature at the surface, ranging between 1600 K and 1900 K, and goes down to the CMB. The temperature of the CMB is set 600 K hotter than the initial adiabatic temperature at the base of the mantle. Table 2 provides a summary of the initial conditions and boundary conditions used, in which both the core temperatures and the corresponding entropies used to set them are provided. At both the surface and core boundaries, the entropy of the mantle's interior smoothly transitions to the fixed entropy using a half-space cooling model with an age of 50 Myrs. An initial sinusoidal perturbation is also prescribed in the entropy field with a $10\,J/K$ magnitude and $l = 23$ wavelength with the intent of not introducing any persistent long-wavelength features into the mantle dynamics as the system evolves through an initial transient state. The initial radial resolution of rectangular finite elements is 128 cells and the angular resolution is 1536 cells.

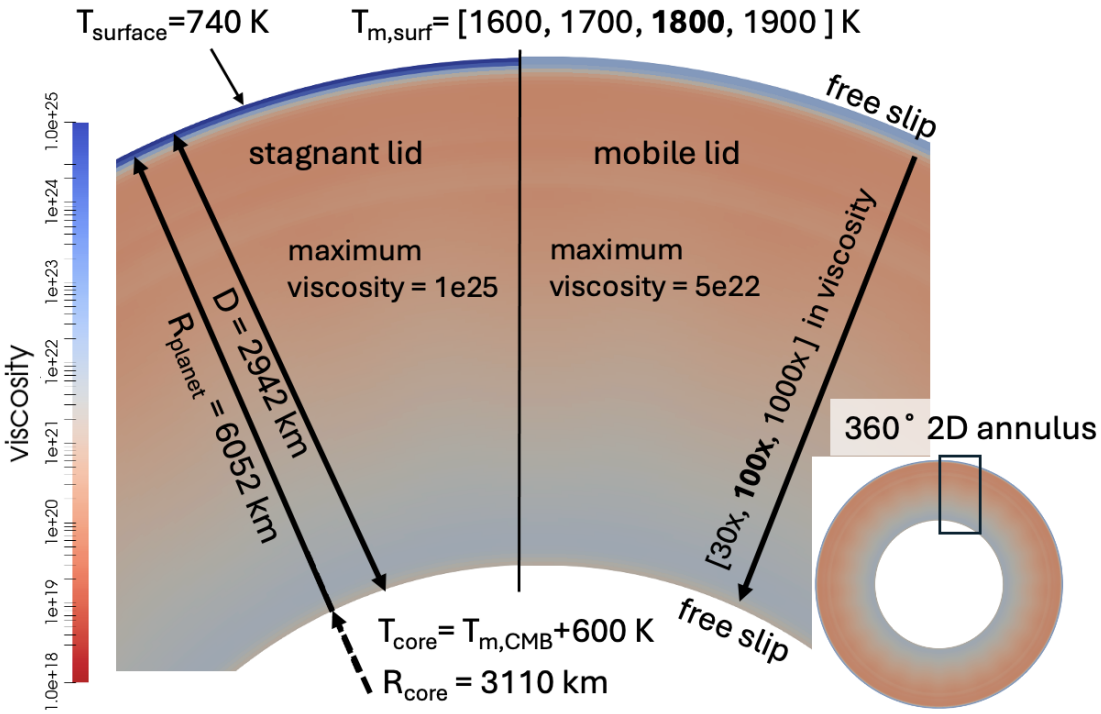

Figure 3: A summary of the initial conditions, boundary conditions, and geometric constraints of the problem in the initial viscosity field for an 1800 K mantle with 100x viscosity increase through the domain. The stagnant lid models (left) and mobile lid models (right) have a maximum viscosity of 10^{25} Pa·s and 5×10^{22} Pa·s, respectively.

Table 2: Summary of initial conditions and variable rheological parameters

Model	$T_{m,0}$ (K)	T_c (K)	S_c (J/K)	Viscosity contrast	V_{act}	$\max \eta$	$H/(nR)$
ML1	1600	3177.97	2802.61	30x	1.84E-06	5e22	33,950.59
ML2	1600	3177.97	2802.61	100x	2.05E-06	5e22	34,548.65
ML3	1600	3177.97	2802.61	1000x	2.47E-06	5e22	35,692.23
ML4	1700	3321.22	2858.38	30x	1.86E-06	5e22	34,014.49
ML5	1700	3321.22	2858.38	100x	2.09E-06	5e22	34,649.07
ML6	1700	3321.22	2858.38	1000x	2.53E-06	5e22	35,861.66
ML7	1800	3486.9	2920.01	30x	1.92E-06	5e22	34,170.78
ML8	1800	3486.9	2920.01	100x	2.16E-06	5e22	34,846.58
ML9	1800	3486.9	2920.01	1000x	2.63E-06	5e22	36,138.98
ML10	1900	3656.08	2980.34	30x	1.98E-06	5e22	34,340.91
ML11	1900	3656.08	2980.34	100x	2.24E-06	5e22	35,059.86
ML12	1900	3656.08	2980.34	1000x	2.74E-06	5e22	36,434.69
SL1	1600	3177.97	2802.61	30x	1.84E-06	1e25	33,950.59
SL2	1600	3177.97	2802.61	100x	2.05E-06	1e25	34,548.65
SL3	1600	3177.97	2802.61	1000x	2.47E-06	1e25	35,692.23
SL4	1700	3321.22	2858.38	30x	1.86E-06	1e25	34,014.49
SL5	1700	3321.22	2858.38	100x	2.09E-06	1e25	34,649.07
SL6	1700	3321.22	2858.38	1000x	2.53E-06	1e25	35,861.66
SL7	1800	3486.9	2920.01	30x	1.92E-06	1e25	34,170.78
SL8	1800	3486.9	2920.01	100x	2.16E-06	1e25	34,846.58
SL9	1800	3486.9	2920.01	1000x	2.63E-06	1e25	36,138.98
SL10	1900	3656.08	2980.34	30x	1.98E-06	1e25	34,340.91
SL11	1900	3656.08	2980.34	100x	2.24E-06	1e25	35,059.86
SL12	1900	3656.08	2980.34	1000x	2.74E-06	1e25	36,434.69
SL13*	1900	3656.08	2980.34	30x	1.98E-06	1e25	34,340.91
SL14*	1900	3656.08	2980.34	100x	2.24E-06	1e25	35,059.86

* linear smoothing of $\log[\text{viscosity}]$ profile through 10-30 GPa

Note: The corresponding entropy used to set the temperature boundary condition is determined using the look-up table at a pressure of 119 GPa and linearly interpolating between the entropy values which bound the desired temperature. Due to the differences in density structure between models with varying potential temperatures, the pressures at the CMB are 119.39 GPa, 118.98 GPa, 118.62 GPa, and 118.22 GPa for the 1600 K, 1700 K, 1800 K, and 1900 K mantles; respectively. Using the pressure of 119 GPa to interpolate the fixed entropy value for the CMB introduces a maximum variation between desired and actual temperatures at the CMB of -7.32 K.

3. Results

In order to investigate the effects of the varying mineral assemblages expected for warmer mantles under the conditions of both a stagnant lid and mobile lid, we produced two nearly identical suites of mantle convection models (of 12 models each). The main difference between the two suites' designs is the maximum viscosity of the lithosphere, which allows for recycling or remains rigid. The range of mantle potential temperatures explored corresponds to a gradual stepping through warmer scenarios in increments of 100 K, starting from an Earth-like mantle temperature of 1600 K. Another parameter of interest is the degree of radial viscosity stratification over the depth of the mantle, because it is also known to significantly influence mantle dynamics. The suites encompass three variations which can be characterized as weak (10x), moderate (100x), or extreme (1000x). A final two models were included to isolate the effect of viscosity variations due to the dependence of the radial viscosity term in Equation 4 on noticeable departures of the adiabatic temperature profile through the transition zone, appearing prominently in the 1900 K models (Figure 2d).

3.1. Mobile lid convection

For all mobile lid models the entropy perturbation in the initial condition leads to an initial system of 23 upwellings and downwellings which become unstable almost simultaneously. This initial instability generates a spike in the surface heat flow as cold plumes form and sink rapidly due to the negative thermal buoyancy of the thick rheological sub-layer, thinning the conductive portion of the lithosphere. This is followed by a spike in the core heat flow corresponding to the cold material from the initial downwellings accumulating on the core-mantle boundary and generating a large thermal gradient across the CMB. The thickness of the cold thermal boundary layer in our mobile lid model varies regionally: thicker around the conduits of descending plumes and thinner above the heads of ascending hot plumes, which heat the base of the lithosphere to mantle temperatures and also laterally displace the mobile lithosphere. As the system evolves towards a steady-state, the number of large upwellings and downwellings reduces as plumes merge and the system relaxes into its natural wavelength of convection.

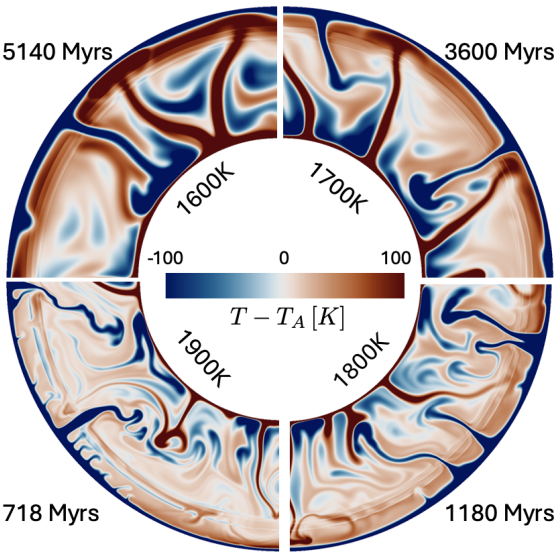

Figure 4: Snapshots of non-adiabatic temperature for mobile lid models ML2, ML5, ML8, and ML11 (clockwise from topleft) at evolved states of their evolution.

Figure 4 shows a characteristic evolved state for mobile lid models with mantle temperatures of 1600 K-1900 K and a viscosity profile with a 100x increase. In the 1600 K and 1700 K models, there is no evidence that mantle phase transitions influence convection dynamics, as upwellings and downwellings pass through the transition zone unimpeded. In the 1800 K model, downwellings passing through the WMF region appear to ”pinch” within that layer, becoming thinner downwellings in the lower mantle. The 1900 K model exhibits the pinching of subducting lower viscosity downwellings as well. They also exhibit a mixture of large, voluminous downwellings with smaller sub-lithospheric drips (also see ML10 in Figure 7) away from the main downwelling conduits resulting in some ephemeral layering. The smaller drips accumulate at a depth between 500-600 km and are flushed from the upper mantle either when a larger, cold downwelling penetrates the transition zone or another strong downwelling drifts and entrains the ponded material into the lower mantle. These accumulations of smaller drips are flushed by larger downwelling flows on timescales that are faster than they can generate their own instability, becoming mixed with the ambient mantle as seen in model ML10 in Figure 7.

In models with 1000x radial viscosity stratification (not shown), instabilities from the hot thermal boundary layer take more time to gain sufficient buoyancy force to push through the lower mantle. As a result, these models tend to have fewer, larger plumes from having spent a prolonged time accumulating boundary layer fluid or having coalesced with adjacent plumes. The cold downwellings from the lithosphere are voluminous and pass through the mantle transition zone without stagnation or layering, mixing the entirety of the mantle.

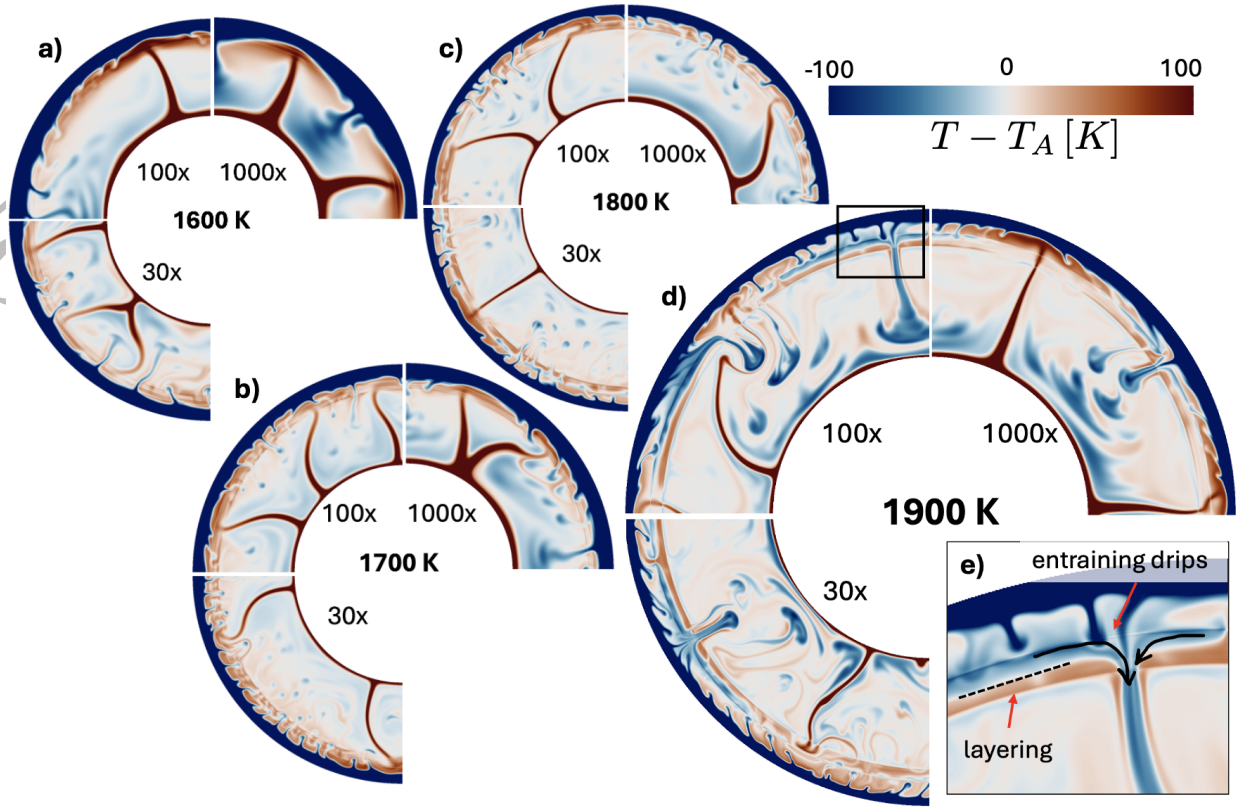

Figure 5: Snapshots at the final time step of stagnant lid models SL1-12 representing the non-adiabatic temperature field of models with initial potential temperatures of a) 1600 K, b) 1700 K, c) 1800 K, and d) 1900 K and mantle viscosity ratios of 30, 100, and 1000. The zoomed-in panel e) shows layering at the base of the WMF region at 600 km depth and cold drips from the lid entrained by the conduit of a mantle avalanche.

3.2. Stagnant lid convection

Figure 5 shows a characteristic evolution for bottom heated stagnant lid models with mantle temperatures of 1600 K-1900 K (models SL1-12) and corresponding CMB temperatures 600 K hotter. Each model evolves from an initial state of 23 hot and cold downwellings, which under stagnant lid conditions produces sub-lithospheric drips spaced $\sim$ 100 km apart with small plume heads and thin trailing conduits. A systematic pattern across the model suite is the presence of inherent asymmetries related to the hot and cold instabilities rising from the respective thermal boundary layers. Instabilities from the underneath the stagnant lid (cold drips) are largest and coldest in the 1600 K models. With increasingly warmer mantles, models show that the cold drips gradually decrease in size, increase in number and frequency, and the magnitude of temperature difference from the adiabat also decreases. In other words, the cold drips have a strong dependence on mantle potential temperature (becoming become noticeably smaller and less potent as mantle potential temperature increases), while the number and frequency hot plumes are much less dependent on mantle potential temperature. The number of hot plumes from the CMB shows a strong dependence on the degree of radial viscosity stratification through the mantle, with larger contrasts resulting in thicker, hotter plumes, but all models tend to have relatively few plumes in total. However, the number and size of cold drips is nearly independent of radial viscosity stratification. In generate, stagnant

lid models like these that are bottom heated and have some degree of radial viscosity stratification exhibit an inherent asymmetry in which there are typically many more cold drips than hot plumes in any given model, and the hot plumes are larger and stronger than the cold drips. However, there is an additional asymmetry in that cold drips are more strongly dependent on these model parameters (mantle potential temperature and radial viscosity stratification) compared to the hot plumes.

Across the entire stagnant lid suite, the 1600 K models have the lowest Ra numbers and thickest lithospheres, resulting in the largest instabilities generated from the thermal boundary layers. These models also have the coldest mantle potential temperature of the suite and at no point does the mantle adiabat cross through the WMF phase region, and unsurprisingly the models do not exhibit any mantle layering. For the 1700 K mantles, the warmer up-welling material appears trapped in and above the transition zone, notably for the 30x and 100x cases which see their average mantle temperatures increase over time. As these mantles get warmer, the temperatures of the lithospheric drips migrate into the WMF zone and are deflected and weakened before entering the lower mantle. The 1800 K models exhibit this behavior to a greater degree as some drips within 100 K of the 1800 K adiabat transform into the WMF phase from wadsleyite (Figure 1b). Still, these cold drips from the lithosphere which see some degree of deflection otherwise pass through to the lower mantle and do not layer (Figure 5c). The presence of the phase transition in the upper mantle of the 1700 K and 1800 K stagnant lid models traps material from the up-welling plumes, increasing the temperature in the upper mantle between 20-100 K globally with respect to the adiabatic profile.

For the stagnant lid models with a temperature of 1900 K, there were no large cold downwellings originating from the cold thermal boundary layer that could individually penetrate the mantle transition zone. The buoyancy of both hot and cold downwellings are weakened by the phase transition into the WMF or OMF (hot plumes only) mineral phases. Since hot plumes are larger and stronger than the cold drips, having had to push through the higher viscosity material in the lower mantle, they pass completely through the phase transition. Conversely, the sub-lithospheric drips layer between 500 km and 600 km depth. The layering is ephemeral and the accumulated material descends into the lower mantle as a mantle avalanche, finally accumulating at the core mantle boundary. A summary of whether or not avalanches were observed in models is provided in Table 3.

3.3. Mantle avalanche dynamics

For models with a 1900 K initial potential temperature, cold drips from the thin rheological sublayer of a stagnant lid planet begin to stall and pond upon reaching the WMF-MF phase transition at 600 km depth (Fig 5e, black dashed line). Because the 1900 K adiabat passes through WMF phase assemblage, the negative thermal expansivity in that zone renders cold material less dense than mantle material below it, making it stably rest atop the WMF-MF transition. Subsequent generations of cold drips from the thermal boundary layer accumulate on top of the cold trapped material from the initial downwellings, as seen in Fig 5e.

The avalanche initiates when the cold, positively-buoyant material trapped within the WMF zone (and subject to a negative thermal expansivity) is pushed far enough downward by some driving force that it leaves the zone of negative expansivity and regains its negative buoyancy. The driving force to initiate an avalanche come from either above the layer, or laterally. When enough cold material has accumulated and ponded above the negative

Table 3: Summary of model results: mantle avalanches, final time, change in mantle temperature at final time, final average surface heat flux, and final average core heat flux

Model	avalanches? (Y/N)	t_f (Myrs)	ΔT_f (K)	$\bar{q}_s$ (mW/m^2)	$\bar{q}_c$ (mW/m^2)
Mobile lid models					
ML1	N	4400.2	-138	36.4	57.6
ML2	N	5100.04	-204	35.7	54.4
ML3	N	3500.05	-189	35.4	41.0
ML4	N	2050.10	-76.3	47.8	68.3
ML5	N	3600.16	-171	42.2	61.1
ML6	N	5950.19	-298	40.2	66.1
ML7	N	920.039	-28.4	58.9	90.4
ML8	N	1320.13	-69.7	53.9	64.1
ML9	N	2440.07	-190	55.5	52.3
ML10	N	540.010	-30.2	76.4	107
ML11	N	715.014	-57.2	71.5	83.7
ML12	N	1225.08	-130	63.3	53.6
Stagnant lid models					
SL1	N	4400.07	41.9	13.0	34.9
SL2	N	3500.19	-22.8	11.0	22.8
SL3	N	5600.77	-86.5	9.64	17.4
SL4	N	2550.10	55.8	16.9	38.9
SL5	N	3700.05	17.1	14.7	31.2
SL6	N	4350.17	-80.7	11.9	23.0
SL7	N	1060.03	14.8	23.6	56.2
SL8	N	1180.03	-9.73	22.0	43.2
SL9	N	1640.09	-53.2	18.2	24.1
SL10	Y	600.022	-3.53	32.7	75.4
SL11	Y	800.005	-26.0	30.1	57.7
SL12	Y	985.04	-67.8	24.3	37.1
SL13*	Y	495.013	-4.95	33.4	77.0
SL14*	Y	620.013	-21.6	30.5	59.6

* linear smoothing of $\log$[viscosity] profile through 10-30 GPa

expansivity zone, producing a regional net negative buoyancy, the bottom portion of the stalled layer is pushed past the lower boundary of the WMF-MF phase boundary. Alternatively, initiation of avalanches can be related to lateral forces driven by adjacent convective motions. Material within the zone of reversed buoyancy is trapped, but also confined within a narrow zone between the two depths of the WMF phase change by hot ponded material on the MF side and cold ponded material on the olivine side. Hot plumes penetrating the WMF zone can displace the trapped material by forcing it to move either laterally or vertically down, generating an unstable perturbation at the WMF-MF boundary and forcing some amount of trapped cold material to pass downwards through the WMF-MF phase transition and its "normal" negative buoyancy in immediately restored to reinforce the larger scale avalanche instability.

The avalanche conduits are cut off as the upwards force of positively-buoyant cold material in the WMF zone competes with suction of entrained upper mantle material that flows laterally towards a smaller conduit of downwelling flow. In the 1000x models, some conduits are thicker since the downwelling velocity is slower and the avalanches are wider. However, since the avalanches descend more slowlhy, there is less entrainment velocity through the WMF zone for material coming through that pathway. It is then easier to decelerate that slower material back to stagnation, and the avalanches in this model last for less time. Additionally, the fewer plumes from the CMB, due to the suppressing effect of high viscosity at depth, generate fewer perturbations on the boundary which means each avalanche has the potential to entrain more material individually than if there were many perturbations. Thus, there is some amount of Stochasticity in the sizes of the avalanches within a single model due to the timing, distribution, and number of hot plumes ascending as well as the past timing, distribution, and number of recent avalanches.

The forces driving the dynamics of the mantle transition zone can be investigated by looking at the estimated buoyancy field in the upper mantle. Changes in the volumetric buoyancy force B are driven by temperature variations from a reference adiabatic temperature T_A. The adiabatic temperature profile and densities along that curve are interpolated from the S-P look-up table at each time step corresponding to the mean entropy of the mantle. The estimated thermal buoyancy field is given by

$$B = \rho_A \alpha g (T - T_A) \tag{5}$$

and represents the effective volumetric force at a given point due to the local temperature, the adiabat, and the thermal expansivity. In Figure 6, the models SL2, SL5, SL8, and SL11 are plotted in the thermal buoyancy field and the color scale is split according to the sign of the thermal expansivity. Most of the mantle fluid shown in Figure 6 has a normal buoyancy by virtue of silicate material having a positive thermal expansion with cold material becoming denser due to thermal contraction (green) and warm material becoming less dense due to thermal expansion (magenta). However, in the 1800 K model (Figure 6c), the hot up-welling plume becomes negatively buoyant (purple) in the transition zone and deflects laterally instead of rising directly upward. Similarly, in the 1900 K model (Figure 6d), the cold drips from the lithosphere (highlighted with black circles) are seen entering the mantle transition zone as green and progressively transforming to orange (positively buoyant with negative thermal expansivity), implying the force on the drip changed from radially downwards to upwards. The reversal of buoyancy occurs across the depth of the WFM phase assemblage. Within the root of an avalanche conduit (Figure 6d, leftmost black circle), material experiencing a reversed sense of buoyancy force (in orange)

actually wants to rise but is viscously-coupled to the downwelling material beneath it. As the downwelling flow is larger, it provides an overwhelming amount of negative buoyancy and successfully entrains the positively buoyant cold material down with it.

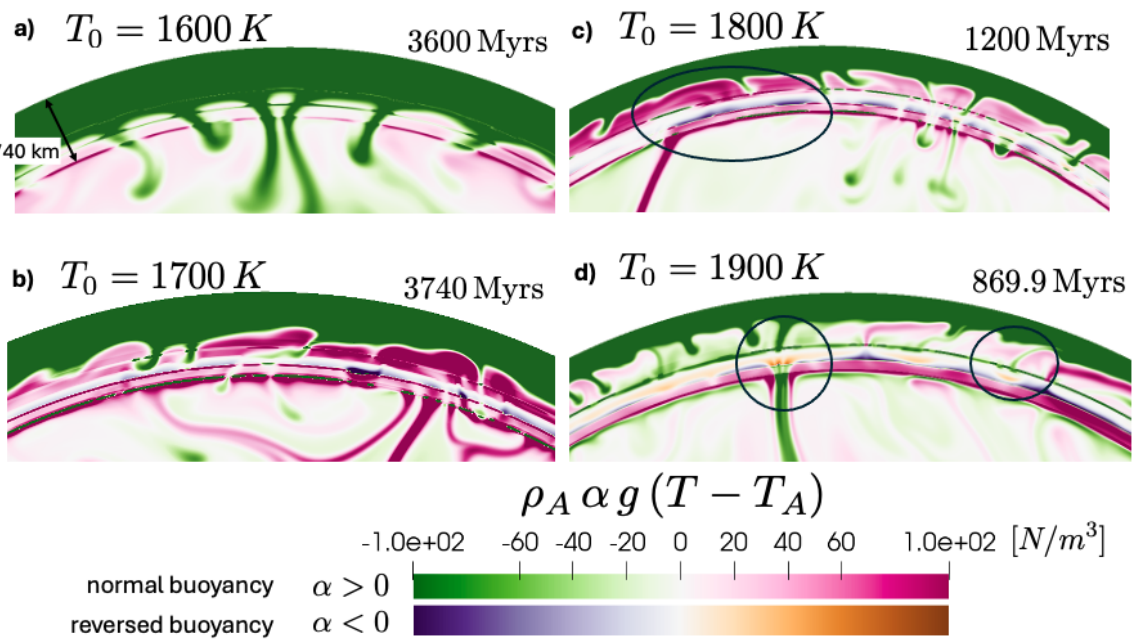

Figure 6: Upper mantle region of stagnant lid models a) SL2, b) SL5, c) SL8, d) SL11 showing estimated buoyancy of mantle with respect to the adiabatic mantle. For material with non-adiabatic temperatures that pass into the WMF transition region, the associated negative thermal expansivity ($\alpha < 0$) makes the buoyancy opposite to normal mantle behavior (shown with the purple-orange colorbar). Location of the Bridgmanite phase transition at 740 km is seen as the deepest of the sequential radial arcs (dark magenta). Circled features indicate regions where c) upwellings and d) downwellings transition through the zone of reversed buoyancy.

Once a perturbation has progressed far enough that a sufficient amount of previously trapped cold material has had its negative buoyancy restored, a larger scale instability (avalanche) develops. The size of this new downwelling is significantly larger than individual cold drips from the lithosphere, and as it sinks into the lower mantle it can entrain remaining adjacent cold material with it, even if that material was otherwise neutrally- or positively-buoyant because it was in the WMF region. These dynamics are shown in the left-most circled region of Figure 6d).

3.4. Mantle avalanches and heat flow

Due to the increased mobility of cold material in a mobile lid model, these models cool more efficiently since a greater volume of mantle material is able to convect. Two-sided symmetric downwellings thin the lithosphere and allow greater surface heat flow despite the core heat flows of stagnant-lid and mobile-lid being more similar. Mobile lid models cool at rates between 30-100 K/Gyr. On the other hand, stagnant-lid planets cool very slowly due to the presence of an immobile conductive lid that traps heat inside the planet, and in some cases actually

warms up because the bottom heating exceeds the cooling through the surface. The temperature change over time of the stagnant lid planets is more variable with most models cooling 5-70 K/Gyr, but 4 models heating up at rates of 5-22 K/Gyr. This variability appears to be most strongly controlled by the degree of radial viscosity stratification, as cases with 1000x viscosity increase with depth suppress plume generation at the CMB, which reduces the associated heat flow from the core and leads to highest rates of secular cooling. The presence of mantle avalanches might increase the overall cooling of the planet. Models with weak radial viscosity stratification (x30) such as SL1, SL4, and SL7 all heating up at 9.5 K/Gyr, 21.9 K/Gyr, and 14.0 K/Gyr, respectively. However, the model SL10 (also 30x) actually shows the opposite and cools at 5.9 K/Gyr. Similarly, for models with moderate radial viscosity stratification (x30), SL5 is warming but SL2 and SL8 are both cooling at -6.5 K/Gyr and -8.2 K/Gyr, respectively, while SL11 is cooling much faster at 32.5 K/Gyr. It seems in both cases the models with avalanches are cooling disproportionately faster for having only a slightly warmer mantle. Although secular cooling in SL10 and SL11 could be enhanced by having a slightly different stagnant lid thicknesses than the other models, in particular during the earlier stages of the systems thermal evolution, the mantle avalanches significantly enhance large scale stirring of the interior which counters the natural thermal stratification of hotter material in the upper mantle of stagnant lid models. The enhanced cooling rates may be a byproduct of the increased thermal mixing of the interior.

3.5. Radial viscosity variations in the transition zone

The mantle adiabats for the 1800 K and 1900 K models exhibit departures from the expected quasi-linear increase with depth due to thermodynamic effects of the WMF phase transition, causing the mantle to get slightly colder with depth instead of warmer (Fig 1a,b). These departures actually cause a corresponding increase (”bump”) in viscosity of about a factor of 4 over over the 600 km - 750 km depth range (Fig 2d). We designed two models (SL13 and SL14) in order to test whether or not this bump in the radial viscosity profile was the singular reason for the ephemeral layering at 600 km depth in the 1900 K stagnant lid models. For these models, all parameters and initial conditions were identical to those in models SL10 and SL11 except for a linear smoothing of the viscosity through the region of the bump (dashed black line in Fig 2d). In Figure 7 we show the results of this test with a side-by-side comparison of SL13 with its twin SL10, as well as the mobile lid version ML10 for reference. There are no distinguishable differences in mantle avalanche formation between models SL10 and SL13 due to the presence or absence of a bump in the radial viscosity profile in the transition region.

From this result we can conclude that the ultimate cause of layering at the WMF-MF phase boundary is due to the thermodynamic properties of the WMF mineral assemblage and not because of the bumps in radial viscosity. Furthermore, model ML10 exhibits ponding of small, cold drips that lead to ephemeral layering atop the WMF-MF phase boundary, as well as a noticeable pinching of larger downwellings that eventually pass through the WMF-MF phase boundary. Although this is indicative of reduced mass flux across the transition zone, the ponding of cold drips in ML10 does not lead to mantle avalanches because larger downwellings occur frequently enough to induce substantial mass exchange which keeps the system well-mixed.

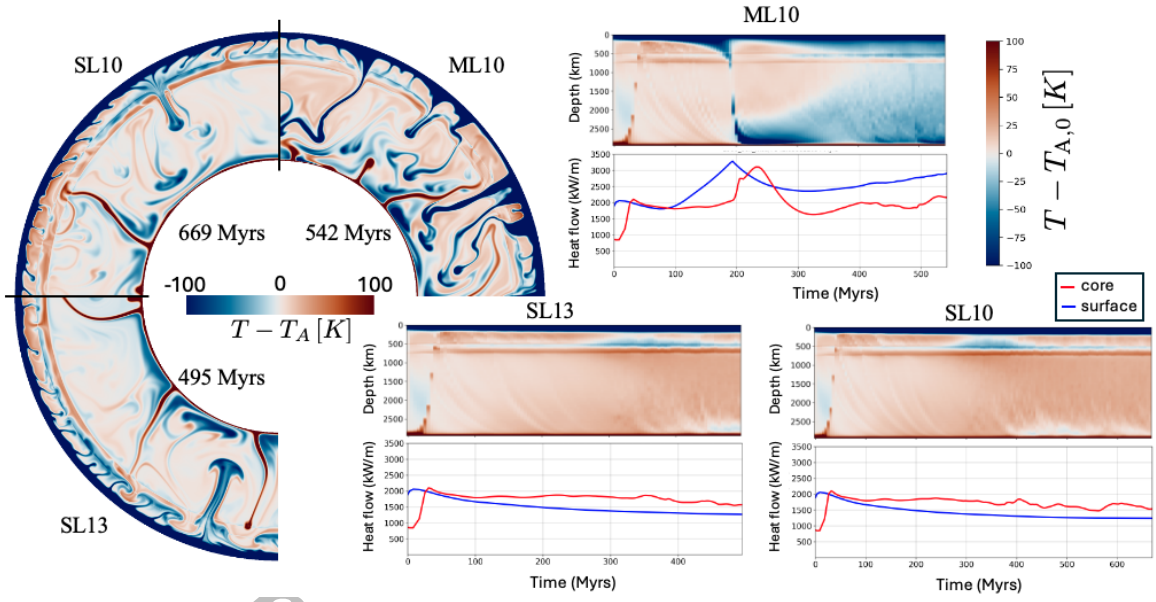

Figure 7: Left: Non-adiabatic temperature field for models SL10, SL13, and ML10, each with initial temperatures of 1900 K and a 30x viscosity increase with depth through the mantle. Right: Depth-averaged temperature deviation from the initial mantle adiabat (top) and the surface and core heat flow evolution (bottom) for models SL10, SL13, and ML10.

4. Discussion

This work follows directly from research conducted in (Dannberg et al., 2022) where the entropy method was first formulated and used. That study used Earth-like geometries and boundary conditions and explored mantle temperatures of 1600 K, 1700 K, and 1800 K. In their 1800 K models, some layering of hot plumes at the transition region was noted, and it was implied that an early Earth could exhibit mantle layering and the stagnation of hot plumes at the upper mantle. The work of (Ichikawa et al., 2014) had previously investigated hot plumes at the WMF-MF transition in a mobile lid regime in the context of an early Earth, and they primarily report increased plume temperatures as much as 100-150 K due to latent heat release from MF to WMF phase change. A more recent study (Li et al., 2024), also within the mobile lid regime, expanded the range of mantle temperatures to include 1900 K with additional consideration of the effects of internal heating. Li et al. (2024) identify a layering regime in which the WMF to MF phase transition impedes up-welling plumes in models with mantle temperatures 1900 K, as long as the system has not experienced enough secular cooling through thermal evolution such that the mantle adiabat no longer crosses into the WMF region. We observe similar behavior in our mobile lid models with warmer initial mantle potential temperatures (>1800 K) while the mantle adiabat crosses into the WMF region (these models cool at an approximate rate of 50-100 K/Gyr). In particular, for the 1900 K models, deflection and stalling of hot plumes, as well as ponding of hot material from plume conduits, is observed to occur below the WMF-MF phase change. Li et al. (2024) provides a schematic diagram how such layering and filtering of plumes might be relevant to different tectonic/volcanic regimes of the early Earth. Additional research into this area is needed, in particular for evaluating the strength and persistence of such laying in the presence of

large downwellings.

The mobile lid regime is defined by global recycling of the lithosphere, and thus incorporates the full thickness of the cold thermal boundary layer and includes the full temperature drop across the surface. Therefore, cold downwellings represent a significant volume of cold material and are capable of much faster cooling of the interior compared to the stagnant lid regime. In our models, and those of Dannberg et al. (2022), it is the reduced maximum viscosity that permits the entire lithosphere to be recycled. We note that in our 1800 K-1900 K mantles, the downwellings appear "pinched" in the WMF region before falling into the lower mantle, perhaps as some type of necking instability that is related to this artificially reduced maximum viscosity of cold material. The models of (Li et al., 2024) were able to achieve recycling of higher viscosity lithosphere by incorporating a plastic rheology which allows yielding of stronger material, however some amount of similar necking appears to be present in those models as well.

Our mobile lid models, as well as those of both (Dannberg et al., 2022) and (Li et al., 2024), observe a partial impedance of mass exchange due to the WMF-MF phase transition. However, such layering is ephemeral because it is easily overwhelmed by the size and rate of the cold downwellings that drive significant return flow and disrupt the gradual build-up of material ponding on either side of the WMF-MF transition. However, in a Venus-like planet with a stagnant lid, the ponding and layering of warm material across the WMF-MF phase change would not disrupted by such large mass exchanges. The smaller drips forming within a thinner rheological sublayer are much weaker and transport smaller temperature differences and correspondingly smaller viscosity contrasts across the base of the stagnant lid and the ambient mantle. In our models with a hotter mantle (1900 K), there is a clear regime shift between downwellings in the mobile lid compared to those in the stagnant lid, indicating that the convective dynamics in a present day Venus could be different those of present-day or early Earth that had a mobile lid.

The magnitude of negative thermal expansivity of the WMF phase assemblage, as well as the extent of P-T space in which it occurs, are both controlling factors in the propensity of a stagnant lid planet to form mantle avalanches. In our model suite that had stagnant lids, the models with warmer mantle temperatures (>1800 K) allowed increasingly stronger layering to occur within the WMF phase region due to the changing nature of material dripping from the lithosphere (i.e. smaller, less cold drips) compared with mobile lid models. The two conditions are thus both well-represented; first, the temperature of the mantle is hot enough that the mantle adiabat intersects with the zone of negative thermal expansivity characteristic of the WMF phase assemblage. Second, the cold deviations from the mantle adiabat ($-50\,K$ to $-200\,K$) mostly remain within P-T space of where the WMF phase assemblage occurs. This means that the temperature of the cold downwellings must not deviate too greatly from that of the ambient mantle that they would no longer be in the WMF region. This condition is better achieved in stagnant lid models, where the temperature drop across the rheological sublayer is a smaller percentage of the temperature drop across the entire lithosphere, compared to mobile lid models. The increased strength of the lithosphere in stagnant lid planets prevents it from participating in convection, and only the rheological sublayer of the lithosphere drips into the upper mantle to interact with the phase transitions. Within our suite of stagnant lid models, all of which use a maximum viscosity of 10^{25} Pa·s, only the 1900 K models were hot enough to have both a mantle adiabat and a significant volume of colder material remaining within the fairly restrictive zone of P-T space occupied by the WMF phase with its negative expansivity.

Mantle avalanches have previously been reported and studied extensively in thermal convection models with the causation of the ephemeral layering and flushing of upper mantle material attributed to the negative Clapeyron slope of the 660 km phase transition of ringwoodite to bridgemenite + ferropericlase (Machetel and Weber, 1991; Solheim and Peltier, 1994; Weinstein, 1993; Honda et al., 1993; Tackley et al., 1993). The early study by (Christensen and Yuen, 1984) of layered mantle convection reported a "leaky" layered state due to mantle phase transitions which necessitated a Clapeyron slope of at least -6 MPa/K. The value of the 660 Clapeyron slope, as well as its uncertainty, has decreased since the earliest studies; with seismic studies (e.g. (Lebedev et al., 2002; Kaneshima et al., 2012)), X-ray diffraction experiments (e.g. (Litasov and Ohtani, 2005; Litasov et al., 2005; Fei et al., 2004; Katsura et al., 2003; Ishii et al., 2011)), and thermodynamic calculations (e.g. (Akaogi et al., 1989)) putting the Clapeyron slope of Earth's 660 km phase transition between -0.5 and -3 MPa/K (Arredondo and Billen, 2016; Yanagisawa et al., 2010). Generally speaking, numerical models which incorporate mineral physics suggest that as the Clapeyron slope of the 660 transition becomes increasingly negative, the mantle becomes increasingly more layered. Other contributing factors such as viscosity stratification in the upper mantle can aid this layering (Yanagisawa et al., 2010; Rudolph et al., 2015).

The flattening and deflection of subducting slabs is considered contemporary evidence for some degree of layering between the upper and lower mantles at the 660; however, recent studies indicate that the negative Clapeyron slope alone may not account for such behavior. Instead the differing morphology of subducting slabs as seen from tomography could depend on a combination of the 660 endothermic transformation, the buoyancy effects of the slow diffusion rate of the transformation of pyroxene to majorite (King et al., 2015), upper mantle viscosity structure, trench retreat rate, and slab dip angle (Torii and Yoshioka, 2007; Goes et al., 2017). In our models, we rule out the effects of viscosity stratification as the cause of the layering and mantle avalanches by comparing models SL13 and SL14 with SL10 and SL11, between which there was no significant dynamical difference. We determine it is the zone of reversed buoyancy causing the layering and avalanches and not a result of a radial increase in the depth-dependent reference viscosity due to sharp changes in the adiabatic temperature at the phase transition. Our analysis documents the dynamics of cold drips from the stagnant lid by estimating the buoyancy field which shows a clear positive buoyancy signal for cold accumulating drips. This analysis suggest it is the negative expansivity of the WMF phase assemblage that generates layering in the models. To our knowledge, no previous studies attribute mantle avalanches to the high temperature phase transition of WMF to MF, particularly due to the exotic nature of thermal buoyancy in the WMF region.

Direct evidence of mantle avalanches occurring inside Earth remains elusive, but the phenomena could be indirectly observed in several ways. Cold, dense, and voluminous instabilities falling into the lower mantle can change the inertial tensor of that body, causing a mis-alignment between the principle axis of inertia and the rotation axis, driving a reorientation of the planet i.e. true polar wander (Machetel and Thomassot, 2002; Moser et al., 1997). There are some examples which could be attributed to large scale flushing of the upper mantle, such as the late Cretaceous rapid true polar wander event which occurred at a rate of 3-10 degrees/Myrs (Sager et al., 2000). This event could be tied to other phenomenon such as large igneous province eruptions and a shift in the magnetic polarity of the Earth (Sager et al., 2000). A mantle avalanche could generate a strong upwards return flow of warmer material into the upper mantle which could enhance seafloor spreading rates and associated volcanism (Machetel and Humler, 2003; Stein and Hofmann, 1994). Alternatively, it could destabilize plume

generation at the CMB by piling sub-critical convecting material into a critical mass, forming a super-plume (Honda et al., 1993). The arrival of an avalanche to the CMB would cause an increase in heat flux locally from the core, and this skewed perturbation in heat flow could have some baring on the duration of strength or direction of Earth's magnetic field, as suggested in (Eide and Torsvik, 1996). The suggestion that mantle avalanches could occur on Venus is new and would need to be investigated further. The presence of multiple large igneous provinces (e.g. the Alta, Beta, and Themis Regios) as well as large regions of deformation (tesserae) could be indicative of strong lateral upper mantle flow associated with the sinking and regional material entrainment into a mantle avalanche.

5. Conclusion

The thermodynamic properties of the WMF phase transition zone correspond to material properties above, below, and through the transition which generate sufficient upper mantle layering to produce mantle avalanches in a stagnant lid Venus with mantle temperatures of 1900 K. The presence or absence of mantle avalanches at different mantle temperatures and within the stagnant-lid regime is robust to sizable changes in the viscosity variation with depth and the existence or absence of strong ($\sim$10x) viscosity variations locally in the mantle transition zone.

The possibility of mantle avalanches occurring in Venus' interior represents a fundamental shift from the expected behavior of mantle convection under stagnant lid (or sluggish lid) conditions. Such avalanches driven by intermittent flushing of cold material ponded within the mantle transition zone, due to the zone of reversed buoyancy, allow for larger, more significant mass transfer and large scale stirring of the mantle compared to stagnant lid convection in the absence of the WMF phase transition. Mantle avalanches could be occurring inside Venus today, or could have played a role earlier in Venus' history when the mantle temperature was warmer than today.

Acknowledgements

The authors thank J. Dannberg and L. Stixrude for helpful discussions. The authors are thankful for support from NASA Award 80NSSC22K0100 and U.S. Department of Energy Computational Science Graduate Fellowship under Award Number DE-SC0022158. Computational resources were provided by Extreme Science and Engineering Discovery Environment (XSEDE), which is supported by National Science Foundation grant number ACI-1053575. This research used resources of the National Energy Research Scientific Computing Center (NERSC), a Department of Energy Office of Science User Facility using NERSC award ASCR-ERCAP0026889.

References

Adams, A. C., Stegman, D. R., Mohammadzadeh, H., Smrekar, S. E., and Tackley, P. J. (2023). Plume-induced delamination initiated at rift zones on venus. *Journal of Geophysical Research: Planets*, 128(10):e2023JE007879.

Adams, A. C., Stegman, D. R., Smrekar, S. E., and Tackley, P. J. (2022). Regional-scale lithospheric recycling on venus via peel-back delamination. *Journal of Geophysical Research: Planets*, 127(10):e2022JE007460.

Akaogi, M., Ito, E., and Navrotsky, A. (1989). Olivine-modified spinel-spinel transitions in the system mg2sio4-

fe2sio4: Calorimetric measurements, thermochemical calculation, and geophysical application. *Journal of Geophysical Research: Solid Earth*, 94(B11):15671–15685.

Armann, M. and Tackley, P. J. (2012). Simulating the thermochemical magmatic and tectonic evolution of venus's mantle and lithosphere: Two-dimensional models. *Journal of Geophysical Research: Planets*, 117(E12).

Arredondo, K. M. and Billen, M. I. (2016). The effects of phase transitions and compositional layering in two-dimensional kinematic models of subduction. *Journal of Geodynamics*, 100:159–174.

Ballmer, M. D., Schmerr, N. C., Nakagawa, T., and Ritsema, J. (2015). Compositional mantle layering revealed by slab stagnation at˜ 1000-km depth. *Science advances*, 1(11):e1500815.

Bangerth, W., Dannberg, J., Gassmoeller, R., and Heister, T. (2020). Aspect v2. 2.0. *Zenodo*.

Benešová, N. and Čížková, H. (2012). Geoid and topography of venus in various thermal convection models. *Studia Geophysica et Geodaetica*, 56:621–639.

Christensen, U. R. (1996). The influence of trench migration on slab penetration into the lower mantle. *Earth and Planetary Science Letters*, 140(1-4):27–39.

Christensen, U. R. and Yuen, D. A. (1984). The interaction of a subducting lithospheric slab with a chemical or phase boundary. *Journal of Geophysical Research: Solid Earth*, 89(B6):4389–4402.

Čížková, H., van Hunen, J., van den Berg, A. P., and Vlaar, N. J. (2002). The influence of rheological weakening and yield stress on the interaction of slabs with the 670 km discontinuity. *Earth and Planetary Science Letters*, 199(3-4):447–457.

Dannberg, J., Gassmöller, R., Li, R., Lithgow-Bertelloni, C., and Stixrude, L. (2022). An entropy method for geodynamic modelling of phase transitions: capturing sharp and broad transitions in a multiphase assemblage. *Geophysical Journal International*, 231(3):1833–1849.

Davaille, A., Smrekar, S., and Tomlinson, S. (2017). Experimental and observational evidence for plume-induced subduction on venus. *Nature Geoscience*, 10(5):349–355.

Eide, E. A. and Torsvik, T. H. (1996). Paleozoic supercontinental assembly, mantle flushing, and genesis of the kiaman superchron. *Earth and Planetary Science Letters*, 144(3-4):389–402.

Faccenda, M. and Dal Zilio, L. (2017). The role of solid–solid phase transitions in mantle convection. *Lithos*, 268:198–224.

Fei, Y., Li, J., Hirose, K., Minarik, W., Van Orman, J., Sanloup, C., van Westrenen, W., Komabayashi, T., and Funakoshi, K.-i. (2004). A critical evaluation of pressure scales at high temperatures by in situ x-ray diffraction measurements. *Physics of the Earth and Planetary Interiors*, 143:515–526.

Fukao, Y. and Obayashi, M. (2013). Subducted slabs stagnant above, penetrating through, and trapped below the 660 km discontinuity. *Journal of Geophysical Research: Solid Earth*, 118(11):5920–5938.

Gassmöller, R., Dannberg, J., Bangerth, W., Heister, T., and Myhill, R. (2020). On formulations of compressible mantle convection. *Geophysical Journal International*, 221(2):1264–1280.

Goes, S., Agrusta, R., van Hunen, J., and Garel, F. (2017). Subduction-transition zone interaction: A review. *Geosphere*, 13(3):644–664.

Hirose, K. (2002). Phase transitions in pyrolitic mantle around 670-km depth: Implications for upwelling of plumes from the lower mantle. *Journal of Geophysical Research: Solid Earth*, 107(B4):ECV–3.

Honda, S., Yuen, D., Balachandar, S., and Reuteler, D. (1993). Three-dimensional instabilities of mantle convection with multiple phase transitions. *Science*, 259(5099):1308–1311.

Huang, J., Yang, A., and Zhong, S. (2013). Constraints of the topography, gravity and volcanism on venusian mantle dynamics and generation of plate tectonics. *Earth and Planetary Science Letters*, 362:207–214.

Ichikawa, H., Kameyama, M., Senshu, H., Kawai, K., and Maruyama, S. (2014). Influence of majorite on hot plumes. *Geophysical Research Letters*, 41(21):7501–7507.

Irifune, T., Nishiyama, N., Kuroda, K., Inoue, T., Isshiki, M., Utsumi, W., Funakoshi, K.-i., Urakawa, S., Uchida, T., Katsura, T., et al. (1998). The postspinel phase boundary in mg2sio4 determined by in situ x-ray diffraction. *Science*, 279(5357):1698–1700.

Ishii, T., Kojitani, H., and Akaogi, M. (2011). Post-spinel transitions in pyrolite and mg2sio4 and akimotoite–perovskite transition in mgsio3: precise comparison by high-pressure high-temperature experiments with multi-sample cell technique. *Earth and Planetary Science Letters*, 309(3-4):185–197.

Ito, E. and Takahashi, E. (1989). Postspinel transformations in the system mg2sio4-fe2sio4 and some geophysical implications. *Journal of Geophysical Research: Solid Earth*, 94(B8):10637–10646.

Jellinek, A. M., Lenardic, A., and Manga, M. (2002). The influence of interior mantle temperature on the structure of plumes: Heads for venus, tails for the earth. *Geophysical research letters*, 29(11):27–1.

Kaneshima, S., Kubo, T., and Yoshioka, S. (2012). Geophysical and mineralogical constraints on the post-spinel transformation for the tonga slab. *Physics of the Earth and Planetary Interiors*, 196:23–31.

Karato, S.-i. and Wu, P. (1993). Rheology of the upper mantle: a synthesis. *Science*, 260(5109):771–778.

Katsura, T., Yamada, H., Shinmei, T., Kubo, A., Ono, S., Kanzaki, M., Yoneda, A., Walter, M. J., Ito, E., Urakawa, S., et al. (2003). Post-spinel transition in mg2sio4 determined by high p–t in situ x-ray diffractometry. *Physics of the Earth and Planetary Interiors*, 136(1-2):11–24.

King, S. D., Frost, D. J., and Rubie, D. C. (2015). Why cold slabs stagnate in the transition zone. *Geology*, 43(3):231–234.

Lebedev, S., Chevrot, S., and van der Hilst, R. D. (2002). Seismic evidence for olivine phase changes at the 410-and 660-kilometer discontinuities. *Science*, 296(5571):1300–1302.

Li, R., Dannberg, J., Gassmoeller, R., Lithgow-Bertelloni, C., and Stixrude, L. (2024). How phase transitions impact changes in mantle convection style throughout earth's history: From stalled plumes to surface dynamics. *Authorea Preprints*.

Litasov, K., Ohtani, E., Sano, A., Suzuki, A., and Funakoshi, K. (2005). In situ x-ray diffraction study of post-spinel transformation in a peridotite mantle: implication for the 660-km discontinuity. *Earth and Planetary Science Letters*, 238(3-4):311–328.

Litasov, K. D. and Ohtani, E. (2005). Phase relations in hydrous morb at 18–28 gpa: implications for heterogeneity of the lower mantle. *Physics of the Earth and Planetary Interiors*, 150(4):239–263.

Lithgow-Bertelloni, C. and Richards, M. A. (1998). The dynamics of cenozoic and mesozoic plate motions. *Reviews of Geophysics*, 36(1):27–78.

Machetel, P. and Humler, E. (2003). High mantle temperature during cretaceous avalanche. *Earth and Planetary Science Letters*, 208(3-4):125–133.

Machetel, P. and Thomassot, E. (2002). Cretaceous length of day perturbation by mantle avalanche. *Earth and Planetary Science Letters*, 202(2):379–386.

Machetel, P. and Weber, P. (1991). Intermittent layered convection in a model mantle with an endothermic phase change at 670 km. *Nature*, 350(6313):55–57.

McNamara, A. K. and Zhong, S. (2004). Thermochemical structures within a spherical mantle: Superplumes or piles? *Journal of Geophysical Research: Solid Earth*, 109(B7).

McNamara, A. K. and Zhong, S. (2005). Thermochemical structures beneath africa and the pacific ocean. *Nature*, 437(7062):1136–1139.

Moser, J., Yuen, D. A., Larsen, T. B., and Matyska, C. (1997). Dynamical influences of depth-dependent properties on mantle upwellings and temporal variations of the moment of inertia. *Physics of the earth and planetary interiors*, 102(3-4):153–170.

Phillips, R. J., Raubertas, R. F., Arvidson, R. E., Sarkar, I. C., Herrick, R. R., Izenberg, N., and Grimm, R. E. (1992). Impact craters and venus resurfacing history. *Journal of Geophysical Research: Planets*, 97(E10):15923–15948.

Reese, C., Solomatov, V., Baumgardner, J., and Yang, W.-S. (1999a). Stagnant lid convection in a spherical shell. *Physics of the Earth and Planetary Interiors*, 116(1-4):1–7.

Reese, C. C., Solomatov, V., and Moresi, L.-N. (1999b). Non-newtonian stagnant lid convection and magmatic resurfacing on venus. *Icarus*, 139(1):67–80.

Rolf, T., Steinberger, B., Sruthi, U., and Werner, S. C. (2018). Inferences on the mantle viscosity structure and the post-overturn evolutionary state of venus. *Icarus*, 313:107–123.

Rudolph, M. L., Lekić, V., and Lithgow-Bertelloni, C. (2015). Viscosity jump in earth's mid-mantle. *Science*, 350(6266):1349–1352.

Sager, W. W., Koppers, and AP, A. (2000). Late cretaceous polar wander of the pacific plate: evidence of a rapid true polar wander event. *Science*, 287(5452):455–459.

Sandwell, D. T. and Schubert, G. (1992). Evidence for retrograde lithospheric subduction on venus. *Science*, 257(5071):766–770.

Schubert, G. and Sandwell, D. (1995). A global survey of possible subduction sites on venus. *Icarus*, 117(1):173–196.

Smrekar, S. E., Davaille, A., and Sotin, C. (2018). Venus interior structure and dynamics. *Space Science Reviews*, 214:1–34.

Solheim, L. P. and Peltier, W. (1994). Avalanche effects in phase transition modulated thermal convection: A model of earth's mantle. *Journal of Geophysical Research: Solid Earth*, 99(B4):6997–7018.

Solomatov, V. (1995). Scaling of temperature-and stress-dependent viscosity convection. *Physics of Fluids*, 7(2):266–274.

Solomatov, V. and Moresi, L.-N. (1996). Stagnant lid convection on venus. *Journal of Geophysical Research: Planets*, 101(E2):4737–4753.

Solomatov, V. and Moresi, L.-N. (1997). Three regimes of mantle convection with non-newtonian viscosity and stagnant lid convection on the terrestrial planets. *Geophysical Research Letters*, 24(15):1907–1910.

Stein, M. and Hofmann, A. (1994). Mantle plumes and episodic crustal growth. *Nature*, 372(6501):63–68.

Steinberger, B. and Calderwood, A. R. (2006). Models of large-scale viscous flow in the earth's mantle with constraints from mineral physics and surface observations. *Geophysical Journal International*, 167(3):1461–1481.

Stixrude, L. and Lithgow-Bertelloni, C. (2005). Thermodynamics of mantle minerals—i. physical properties. *Geophysical Journal International*, 162(2):610–632.

Stixrude, L. and Lithgow-Bertelloni, C. (2011). Thermodynamics of mantle minerals-ii. phase equilibria. *Geophysical Journal International*, 184(3):1180–1213.

Tackley, P. J., Stevenson, D. J., Glatzmaier, G. A., and Schubert, G. (1993). Effects of an endothermic phase transition at 670 km depth in a spherical model of convection in the earth's mantle. *Nature*, 361(6414):699–704.

Thiriet, M., Breuer, D., Michaut, C., and Plesa, A.-C. (2019). Scaling laws of convection for cooling planets in a stagnant lid regime. *Physics of the Earth and Planetary Interiors*, 286:138–153.

Torii, Y. and Yoshioka, S. (2007). Physical conditions producing slab stagnation: Constraints of the clapeyron slope, mantle viscosity, trench retreat, and dip angles. *Tectonophysics*, 445(3-4):200–209.

Uppalapati, S., Rolf, T., Crameri, F., and Werner, S. (2020). Dynamics of lithospheric overturns and implications for venus's surface. *Journal of Geophysical Research: Planets*, 125(11):e2019JE006258.

van der Hilst, R. and Seno, T. (1993). Effects of relative plate motion on the deep structure and penetration depth of slabs below the izu-bonin and mariana island arcs. *Earth and Planetary Science Letters*, 120(3-4):395–407.

Weinstein, S. A. (1993). Catastrophic overturn of the earth's mantle driven by multiple phase changes and internal heat generation. *Geophysical Research Letters*, 20(2):101–104.

Widemann, T., Smrekar, S. E., Garvin, J. B., Straume-Lindner, A. G., Ocampo, A. C., Schulte, M. D., Voirin, T., Hensley, S., Dyar, M. D., Whitten, J. L., et al. (2023). Venus evolution through time: key science questions, selected mission concepts and future investigations. *Space Science Reviews*, 219(7):56.

Yanagisawa, T., Yamagishi, Y., Hamano, Y., and Stegman, D. R. (2010). Mechanism for generating stagnant slabs in 3-d spherical mantle convection models at earth-like conditions. *Physics of the Earth and Planetary Interiors*, 183(1-2):341–352.